Energy &
Environmental
Science

Anionic Redox Induced Anomalous Structural Transition in Ni-rich Cathodes

Journal:	*Energy & Environmental Science*
Manuscript ID	EE-ART-09-2021-002987
Article Type:	Paper
Date Submitted by the Author:	23-Sep-2021
Complete List of Authors:	Liu, Jue; Oak Ridge National Laboratory, Chemical and engineering Materials Du, Zhijia; Oak Ridge National Laboratory, Energy & Transportation Science Division; Oak Ridge National Lab Wang, Xuelong; Brookhaven National Laboratory, Chemsitry Tan, Sha; Brookhaven National Laboratory, Chemistry Wu, Xianyang; Oak Ridge National Laboratory; Purdue University Geng, Linxiao; Oak Ridge National Laboratory, Song, Bohang; Oak Ridge National Laboratory, Neutron Scattering Division Chien, Po-Hsiu; Oak Ridge National Laboratory, Neutron Scattering Division Everett, Michelle; Oak Ridge National Laboratory, Spallation Neutron Source Hu, Enyuan; Brookhaven national lab., ; Brookhaven National Laboratory, Chemistry Department

SCHOLARONE™
Manuscripts

Anionic Redox Induced Anomalous Structural Transition in Ni-rich Cathodes

Jue Liu,[a,#,*] Zhijia Du,[b, #] Xuelong Wang,[c] Sha Tan,[c,d] Xianyang Wu,[b,e] Linxiao Geng,[b] Bohang Song,[a] Po-Hsiu Chien,[a] S. Michelle Everett[a], Enyuan Hu[c]

[a] *Neutron Scattering Division, Oak Ridge National Laboratory, Oak Ridge, TN 37831, USA*

[b] *Energy and Transportation Science Directory, Oak Ridge National Laboratory, Oak Ridge, TN 37831, USA*

[c] *Chemistry Division, Brookhaven National Laboratory, Upton, NY 11973, USA*

[d] *Department of Materials Science and Engineering, Stony Brook University, Stony Brook, NY 11974, USA*

[e] *School of Mechanical Engineering, Purdue University, West Lafayette, IN 47907, USA*

Correspondence: liuj1@ornl.gov

# These authors contributed equally

Broad context: High energy density Li-ion batteries with lower cost and longer lifetimes are needed to meet the increasing demands of electric vehicles and smart grids. Cathode materials are widely recognized as the major bottleneck. Ni-rich layered cathodes are emerging as the most promising candidate because of their high capacity and low cost. However, they often suffer from poor cycling performance when charged to high voltages. The degradation mechanism remains elusive and controversial, in large part due to the complex interplay phenomena such as macrocracking, surface reconstruction, surface parasitic reaction and oxygen evolution etc. Thus, identifying the fundamental origin besides the phenomenological observation becomes critical in revealing the hidden driving force underlying the degradation. Here, by using high throughput *operando* neutron diffraction, we discovered the severe capacity degradation of Ni-rich cathodes is universally rooted in an anomalous anonic oxygen redox induced structural transition at ~ 75%

1

charge irrespective of Ni/substituent contents. These findings provide fundamental insights for stable cycling of Ni-rich cathodes at high state-of-charge.

Abstract: Ni-rich cathodes have emerged as one of the most promising candidates to power next generation electric vehicles. However, they often suffer from poor capacity retention when charged to high voltages and the origin of this degradation remains elusive. Here, by using high throughput *operando* neutron diffraction, a universal four-stage structural evolution of Ni-rich cathodes is revealed during the initial cycle for the first time. Particularly, we discovered a universal structural transition in Ni-rich cathodes at ~ 75% delithiation irrespective of Ni or substituent contents. This transition is hallmarked by the anomalous increase of average TM-O bond lengths, contradicting the conventional wisdom that TM-O bond lengths decrease during charge (oxidation). This anomaly is induced by the direct oxidation of lattice oxygen ions, which is rooted in the drastic decrease of oxygen-to-TM charge transfer gap at high degrees of delithiation. The onset of this anomalous transition matches very well with the onset of oxygen gas release and severe decline of capacity retention in Ni-rich cathodes, suggesting this bulk structural transition plays an indispensable role in the degradation process. These findings shed light on the elusive degradation mechanism of Ni-rich cathodes, providing valuable clues to stabilize oxidized oxygen ions for stable cycling of layered oxide cathodes at high voltages.

1. Introduction

Li-ion batteries (LIBs) are broadly used to power portable electronic devices and they are expected to play key roles in the emerging market of electric vehicles.[1] Cathode materials have been widely recognized as one of the major bottlenecks because of their relative low energy density and high cost.[2-4] Among various candidates, cation substituted $LiNiO_2$ with general formula of $LiNi_xMn_yCo_zO_2$ (NMC) or $LiNi_xCo_yAl_zO_2$ (NCA) are the dominant cathodes because of their high energy density and relative low cost.[5-9] Unfortunately, they often suffer from poor capacity retentions when cycled at high cut-off voltages (or at high degrees of delithiation, e.g., > 80%).[10]

Therefore, tremendous amounts of efforts have been devoted to understanding the origin of this degradation in order to achieve higher reversible capacity without sacrificing the cyclability. Despite steady progress, the detailed mechanism is still fiercely debated, and the most widely adopted explanations include: (1) microcracking induced by the accumulation of large amounts of stress/strain during prolonged cycling,[10-15] which has been broadly ascribed to the anisotropic collapse of unit cell volume and lithium concentration gradients at an high state-of-charge (SOC);[10, 16, 17] (2) surface parasitic reactions, surface structure reconstruction, bulk fatigue and cation dissolution;[18-24] (3) oxygen evolution and cation migration[25-27] and (4) undesired phase transition similar to the original H2 to H3 phase transition in the parent compound $LiNiO_2$.[10] Although these explanations seem to be scattered from very different aspects (e.g., mechanic properties, surface or bulk structural transitions etc.), they are all strongly correlated with the status of lattice oxygen ions (e.g., stacking sequences, interlayer Coulomb repulsion, oxidation states and vacancies). Therefore, a comprehensive understanding of the structural evolution, especially those centered on lattice oxygen ions is critical in resolving these long-standing controversies.

To capture the accurate structural changes around lattice oxygen ions, a bulk structure probe that is highly sensitive to light elements is desired. In addition, *operando* evidence obtained during cycling is also critical because of the metastability of deeply charged layered oxide cathodes.[28] *Operando* neutron diffraction is an ideal tool to tackle the above problem: (1) neutron scattering is highly sensitive to light elements such as O, which is critical for the current study; (2) nuclear scattering lengths do not decrease with increasing wave vector (Q), enabling accurate determination of occupancies and atomic displacements of light elements; (3) neutron scattering is less destructive relative to the high energy X-ray diffraction. Thus, it effectively avoids generating heat and disturb electrochemical reactions in battery cells, which may cause inhomogeneous electrochemical reactions (e.g., delayed observation of phase transition etc.).[29] Despite these advantages, the development of *operando* neutron diffraction for battery studies have encountered enormous challenges. The biggest hurdle is the much lower neutron flux at most neutron diffractometers relative to X-ray diffractometers.[30-36] To compensate this effect, much

larger amounts of samples (hundreds of milligrams to grams) or longer counting times are often required. This leads to the design of various *in situ* cells with much higher loadings of active materials (including commercial cells) for neutron diffraction.[33, 36] However, even with large loadings of
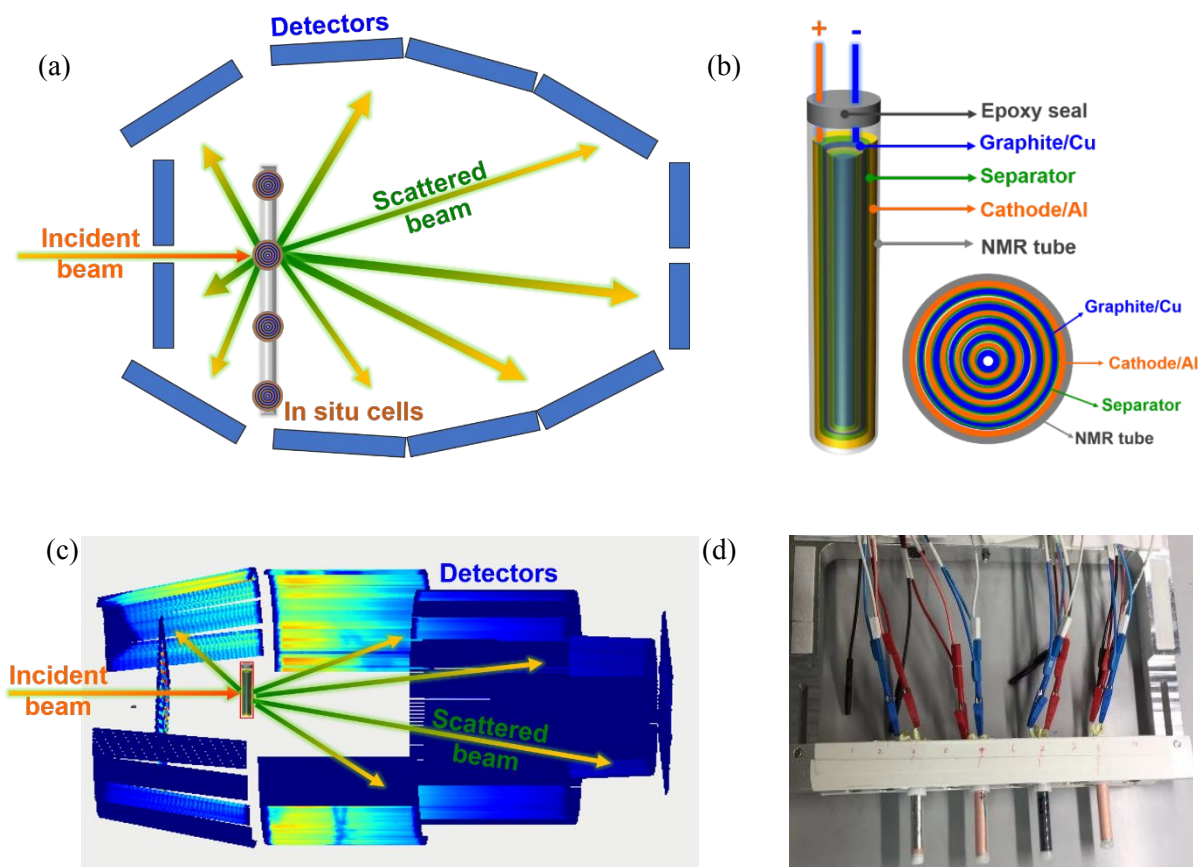

Figure 1. (a) Schematic top view of the high throughput *operando* neutron diffraction study of Li-ion batteries at NOMAD. Four *in situ* cells are mounted on a shift bracket and data collection are carried out sequentially. Six detector banks at NOMAD are centered at $2\theta = 6.7°$, $15°$, $31°$, $65°$, $122°$ and $154°$ separately. Diffraction data collected on the last four detector banks are used for structure analysis. (b) Schematic of newly designed *in situ* cylindrical cell, top view of the jelly roll configuration is also inserted. (c) 3D view of the *operando* neutron diffraction experiment with detectors illuminated. (d) A picture showing $LiNi_{0.8}Mn_{0.1}Co_{0.1}O_2$ (NMC811), $LiNi_{0.8}Co_{0.15}Al_{0.05}O_2$ (NCA), $LiNi_{0.6}Mn_{0.2}Co_{0.2}O_2$ (NMC622) and $LiNi_{0.5}Mn_{0.3}Co_{0.2}O_2$ (NMC532)-graphite full cells (from left to right) on a shift bracket for *operando* neutron

diffraction experiment. Cells were cycled at ~ a C/10 rate (10h charge and 10h discharge) between 2.8 V and 4.6 V. More details about cell design and *operando* experiment are shown in Figure S1.

active materials, collecting high quality neutron diffraction data with high time resolution are still challenging and has only been achieved recently.[29, 36] In addition, high throughput *operando* measurements (of multiple cells) are required to thoroughly investigate the long-believed composition-dependent (e.g., Ni contents) properties of Ni-rich cathodes.[37] To the best of our knowledge, this highly desired capability has not been achieved previously. Recently, we have successfully commissioned the first high throughput *operando* neutron diffraction studies of batteries at the Spallation Neutron Source (SNS)'s Nano-Scaled Materials Diffractometer (NOMAD).[38, 39] The very high neutron flux together with large detector coverage of NOMAD allows for fast data collection of structural refinable neutron diffraction data using our newly designed *in situ* electrochemical cell (Figures 1 and S1). The successful development of this capability motivates us to carry out the following systematic investigation of the long-pursuit structural transition mechanism of Ni-rich cathodes.

In this report, a universal four-stage structural evolution mechanism for Ni-rich cathodes is revealed using high throughput *operando* neutron diffraction. Particularly, we discovered an anomalous increase of average TM-O bond lengths when more than ~ 0.75 Li^+ are removed during the initial charge, and this transition is fully reversible during discharge. This anomalous structural transition is strongly correlated with the oxygen gas release and the universal decline of capacity retention in Ni-rich cathodes, suggesting this overlooked bulk structural transition may play an indispensable role in the degradation process. A comprehensive model has been proposed to explain this anomalous transition and its implication for stable cycling of layered oxide cathodes at high SOCs.

2. Results

2.1 *Ex situ* structure studies of NMCs and NCA

Rietveld refinements of structures of pristine NMCs and NCA were carried out using powder neutron diffraction data. The refinement results are shown in Figures S2-S5 and Tables S1-S5. Lattice parameters refined for NCA are slightly smaller relative to NMCs because of the much smaller ionic radii of Al^{3+} (0.53 Å),[40] this has been further confirmed by the shorter average TM-O bond length refined for NCA (Table S1). Similar Li-O bond lengths (2.11 Å) and LiO_2 slab thickness (2.62 Å) have been observed for all samples, indicating that lithium coordination environments are very similar among these four samples. In addition, the amount of Ni_{Li} anti-site defects (Ni in the TM layer and Li in the lithium layer swap their sites) increases as Ni concentration decreases (Table S1). This value increases from 0.8% in NCA to 4.2% in NMC532. The formation of anti-site defects in various Ni-containing layered cathodes has been largely attributed to the similar ionic radii between Ni^{2+} (0.69 Å) and Li^+ (0.76 Å).[41] The overall trend of our refinement results is in line with this classic argument. However, it is worth noting that several recent studies reported that the super-exchange interaction between anti-site Ni^{3+} and Ni^{3+} in the TM layer as well as the average ionic radii of cations (in the MT layer) may also affect the concentration of Ni_{Li} anti-site defects in Ni-rich cathodes.[42, 43] Consequently, the concentration of this anti-site defect likely strongly depends on the synthetic history of specific batch of samples. These refinement results are used to benchmark the quality of our *operando* diffraction data.

2.2 High throughput *in situ* neutron diffraction study

The schematic of *operando* neutron diffraction studies of $LiNi_{0.5}Mn_{0.3}Co_{0.2}O_2$ (NMC532), $LiNi_{0.6}Mn_{0.2}Co_{0.2}O_2$ (NMC622), $LiNi_{0.8}Mn_{0.1}Co_{0.1}O_2$ (NMC811) and $LiNi_{0.8}Co_{0.15}Al_{0.05}O_2$ (NCA) is shown in Figure 1. *In situ* cells are cycled at a rate of C/10. Diffraction patterns are collected every 4 minutes for each cell in a sequential manner with the average motor moving time of 20s between each cell. Therefore, this *operando* experiment allows monitoring the composition change (ΔLi) of 0.022-0.025 Li^+/formula/scan for all four samples. It could thus effectively capture the structural evolutions of both cathode and anode in a high throughput model. *Operando* neutron diffraction data (highest resolution bank, *2θ* centered at 154°) collected during the first cycle are shown in Figures 2 and S6-S9. The corresponding first galvanostatic charge and discharge curves

are displayed in the middle panel of Figure 2. Regions near the graphite (anode) 114 reflection (d spacing around 1.04 Å) and the NMCs/NCA cathode 110 and 108 reflections (d spacing around 1.45 Å) are selectively shown in contour plots on the right side of Figure 2. The strongest diffraction peaks of Al and Cu (current collectors) are also highlighted.
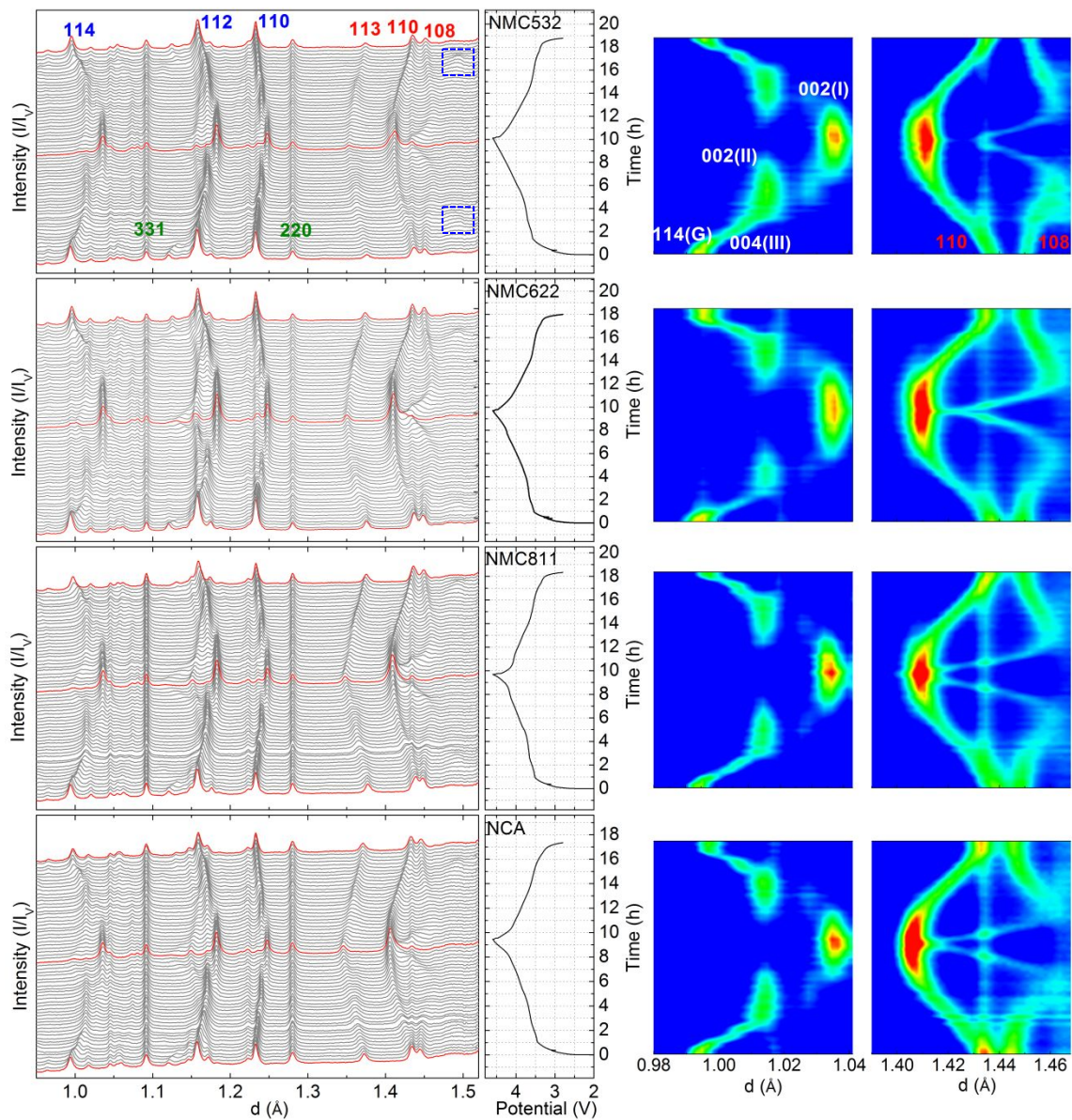
Figure 2. Left, *operando* neutron diffraction data (highest resolution bank, center $2\theta = 154°$) of NMC532, NMC622, NMC811 and NCA (against graphite anode) collected during the initial charge and discharge. The electrochemistry data are shown beside the diffraction data (middle). Right, the evolution of graphite 114 reflection and NMCs/NCA 110 and 108 reflections (in contour plots) during the first cycle. Some key Bragg reflections of NMCs/NCA, graphite and Cu are labeled in red, blue and olive respectively. The dotted blue boxes highlight the evolution of the stage III phase (007 reflection) of lithium intercalated graphite.

Since carbon is a strong neutron scatter and corresponding diffraction peaks of (lithiated) graphite overlaps with those from NMCs/NCA, an accurate monitoring of the structure evolution of graphite anode is critical for achieving reliable structure refinements of NMCs/NCA cathodes. Detailed analysis of structure evolution of graphite during lithiation/delithiation is summarized in the supporting information (section S3). In contrast to the complex multiple two-phase transitions of graphite lithiation, the delithiation of NMCs and NCA (cathodes) follow a solid solution reaction path during the entire charging process, as evidenced by the continuous shift of corresponding diffraction peaks. It is worth noting that a limited two-phase co-existence region has been observed at SOCs between 0 and ~30% for compounds with high Ni concentrations (NMC811 and NCA). This was also reported in previous *in situ* XRD studies .[21, 44, 45] It is now generally agreed the co-existence of two-phases is due to the presence of surface Li_2CO_3, which drastically reduces lithium diffusivity during the initial lithium removal.[45] The formation of this phase is highly correlated with sample storage environment. Materials stored in inert or dry atmosphere are found to possess much less surface Li_2CO_3, in good agreement with the very limited two-phase regions observed in the current study. Since this limited two-phase region does not affect the conclusion of this study, which focuses on the structural evolutions at high SOCs, the refinements of the cathode structures are thus carried out using a single-phase model. Qualitatively, it can be seen that the 110 reflection shifts continuously toward the smaller d-spacing for all four samples (Figure 2), indicating that *ab* plane shrinks during initial delithiation. In contrast, the 108 reflection shifts to the larger d-spacing initially but switches to the opposite direction after removing about 0.5 Li^+ per formula unit (Figure 2), suggesting the *c* lattice expands initially but starts to decrease at about 50% delithiation. Moreover, the *h0l* reflections broaden

8

drastically after removing about 0.5 Li$^+$ while the reflections associated with the in *ab*-plane diffraction (e.g., 110) remain relatively sharp (Figures 2 and S6-S9) through the entire charging process, implying that the anisotropic peak broadening is very likely caused by the stacking disorder along the crystallographic *c*-axis.[46]
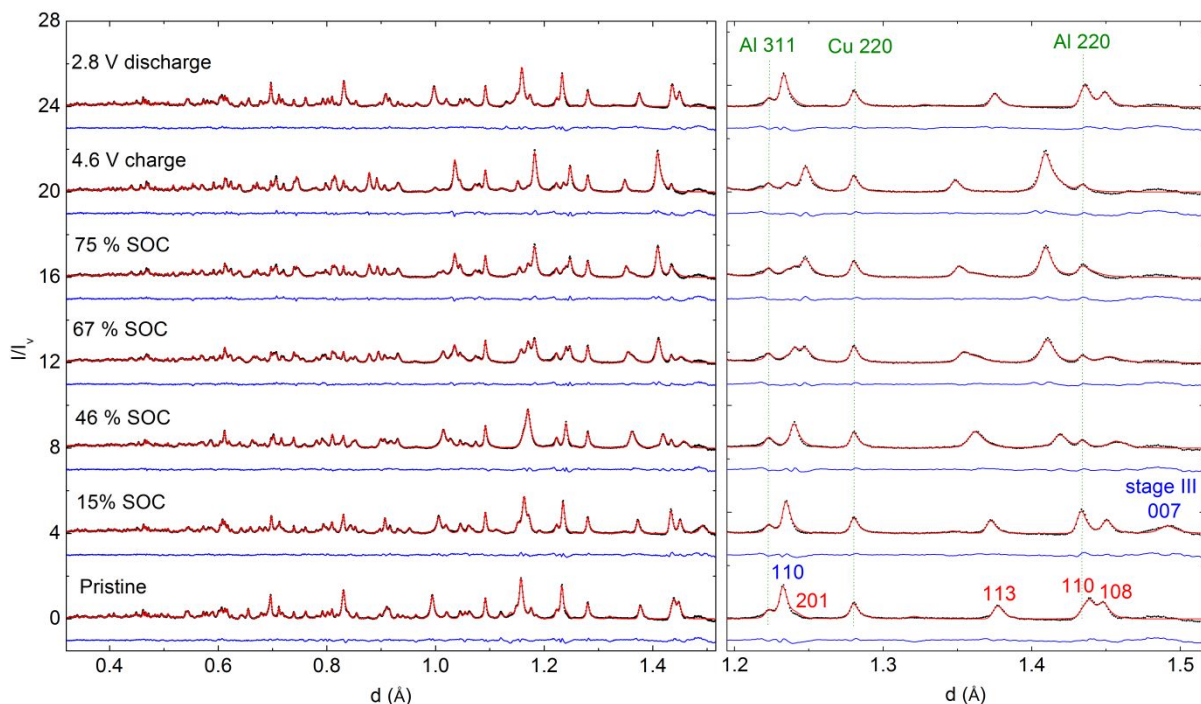

Figure 3. Left, selected Rietveld refinements of NMC811/graphite cell (NMC811, graphite/lithiated graphite, Cu and Al) using *operando* neutron diffraction data (highest resolution bank, center at $2\theta = 154°$) collected at SOCs of 0%, 15%, 54%, 67%, 75%, the end of charge (4.6 V) and the end of discharge (2.8 V). Right, enlarged regions showing some key Bragg reflections of NMC811 (red), graphite (blue), Cu and Al (highlighted in dotted olive lines). Experimental data, calculated data and difference are shown in black, red and blue. Backgrounds are subtracted for clarity. Refinement results for the other compositions are shown in Figures S6-S33.

While qualitative analysis provides useful information about the potential phase transition of Ni-rich cathodes, quantitative analysis is highly desired to gain insights into the relationship between structure and electrochemical properties. To examine whether the quality of the current

in situ data support reliable structure refinements, individual Rietveld refinements of the pristine structures were carried out using initial scans (collected before charging). Four different phases, including NMCs/NCA (S.G. R-3m), graphite (S.G. $P6_3$mm), Cu and Al were included in the refinement. Final Rietveld refinements of the pristine NMC/NCA structures using *in situ* diffraction data are shown in Figures 3 (NMC811), S10-S13 and Tables S6-S10. The refined pristine structures are very similar to those refined from pristine powder samples (Tables S1-S5). In all, this confirms that accurate structure information can be obtained from the quantitative analysis of current *operando* neutron diffraction data.

Parametric Rietveld refinements[47] were carried out for all four cells (detailed methods are described in experiment section), and the corresponding refinement results are shown in Figures S38 - S41. Selected refinement results for NMC811 at SOCs of 0%, 15%, 54%, 67%, 75%, the end of charge (4.6 V versus graphite) and discharge (2.8 V) are shown in Figures 3 (results for other compositions are shown in Figures S10 - S39). Good qualities of fits have been achieved for diffraction patterns collected at different states of charge or discharge, as can be seen from the relatively low R_{wp}, GOF (goodness of fit) and relatively flat difference curves (Figures S10-S39 and S42). The slight change of the refinement residual values as a function of SOCs is due to the emerging/disappearing of bi-phasic regions of lithium intercalated/deintercalated graphite (staging phases). The refined lattice parameters and unit cell volumes of NMCs and NCA are plotted as a function of the state of charge and discharge (Figure 4). Similar trends have been observed for all four samples: *a* lattice decreases continuously until about 54% - 56% delithiation (note the composition resolution is about 2% Li^+/formual unit), and it then plateaus during further delithiation before starting to slightly increase at SOCs above 74% - 76%. In contrast, *c* lattice expands initially until reaching about 54% - 56% delithiation. It then plateaus during further delithiation and eventually collapses when more than 67% - 70% Li^+ are removed. The unit cell volume continues decreasing during the initial charge but at substantially different rates before and after ~ 67% delithiation. Since the cell volume is proportional to $a^2 * c$, the volume contraction in the first stage (< ~67% delithiation) is predominantly driven by the decrease of *a*-lattice (or *ab*

plane dimension). On the other hand, the collapse of cell volume above 67% delithiation is due to the drastic decrease of *c*-lattice. It is worth noting that the relative ratio of volume contraction (normalized to the initial cell volume, Figure S43) are similar among all four samples (with slight Ni-concentration dependence), suggesting that there is likely a universal mechanism governing the anisotropic volume change in Ni-rich cathodes irrespective of their Ni or substituent contents. In addition, it also implies that the macroscopic strain/stress induced by cell volume collapse may follow a comparable trend in all four samples at the same degree of delithiation, in good agreement with the previous observations from XRD studies. [16, 17]
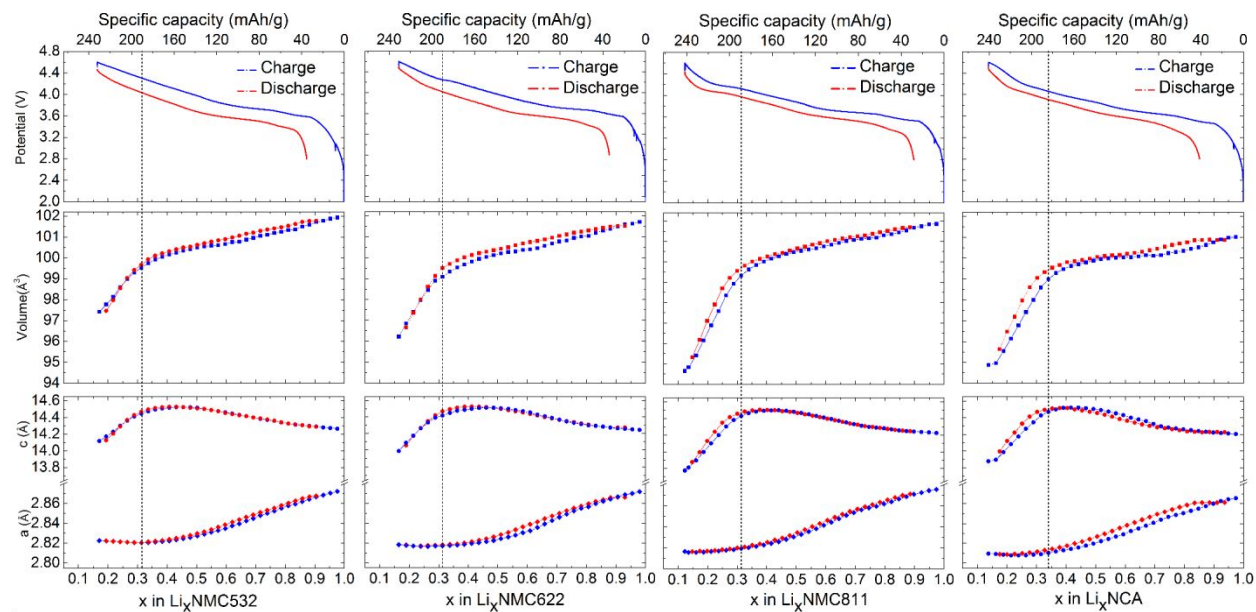

Figure 4. Evolution of lattice parameters and unit cell volumes of NMC532, NMC622, NMC811 and NCA as a function of the state of charge and discharge. *a*-lattice decrease monotonically during initial charge and plateaus (or slightly increase) at SOCs around 67%-70% (x ~ 0.30-0.33). In contrast, *c*-lattice increases initially upon charging but plateaus at SOCs around 54%-56% (x ~ 0.44-0.46). It starts to collapse when approaching SOCs of 67%-70%, resulting in the collapse of cell volume (highlighted in dotted line).

2.3 Anomalous increase of TM-O bond lengths at SOCs above 75%

To further understand the structural change of NMCs/NCA cathodes during the initial charge/discharge, the evolution of Li-O and TM-O bond lengths are shown as a function of the

degree of delithiation in Figure 5. The average Li-O bond distance continues increasing at SOCs below 54% - 56% but starts to plateau out upon further Li^+ removal, in line with the trend of c-lattice (Figure 4). However, it is worth noting that the turning point (switching from increase to decrease) of Li-O bond lengths does not necessarily match the turning point of c-lattice or cell volume (details in supporting information S2). It turns out that the turning points of Li-O bond lengths in NMC532 and NCA match well with the corresponding turning points for c-lattice. However, the turning points of Li-O bond lengths for NMC622 and NMC811 are at higher degrees of delithiation (74% - 76%) (details in supporting information S2). Meanwhile, the TM-O bond distances show an interesting feature such that they continuously decrease until about 74-76% delithiation but then start to increase (instead of decrease) upon further delithiation. Moreover, similar universal turning points (SOC of 74% - 76%) have been observed for thickness of TMO_2 slabs (Figure 5), O-TM-O angles (Figure S44), and interlayer O-O distances across the TMO_2 slabs (Figure S44).
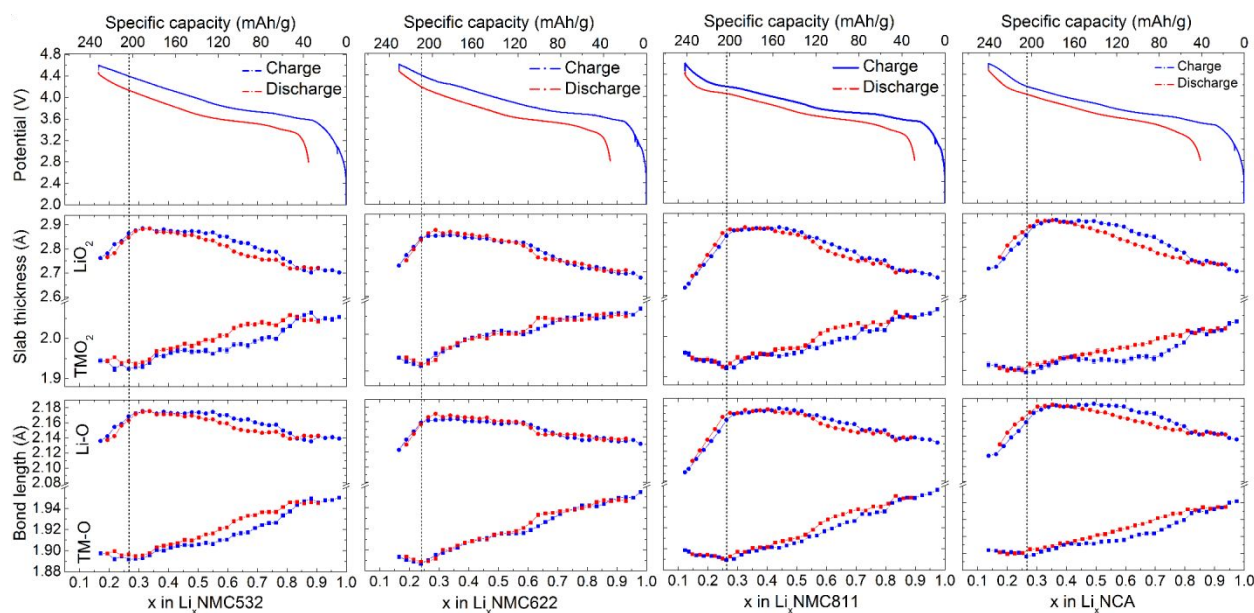

Figure 5. Evolution of TM-O, Li-O bond lengths, LiO_2 and TMO_2 slab thickness of NMC532, NMC622, NMC811 and NCA during the initial cycle. Both Li-O bond length and LiO_2 slab thickness increase during charge until about 50% delithiation, they then start to plateau out during further delithiation and eventually

collapses at about 67%-70% delithiation. In contrast, TM-O bond length and TMO_2 slab thickness decrease monotonically until about 74%-76% delithiation but then start to increase during further delithiation (highlighted in dotted line). Structure changes are reversible during discharge despite some degrees of hysteresis.
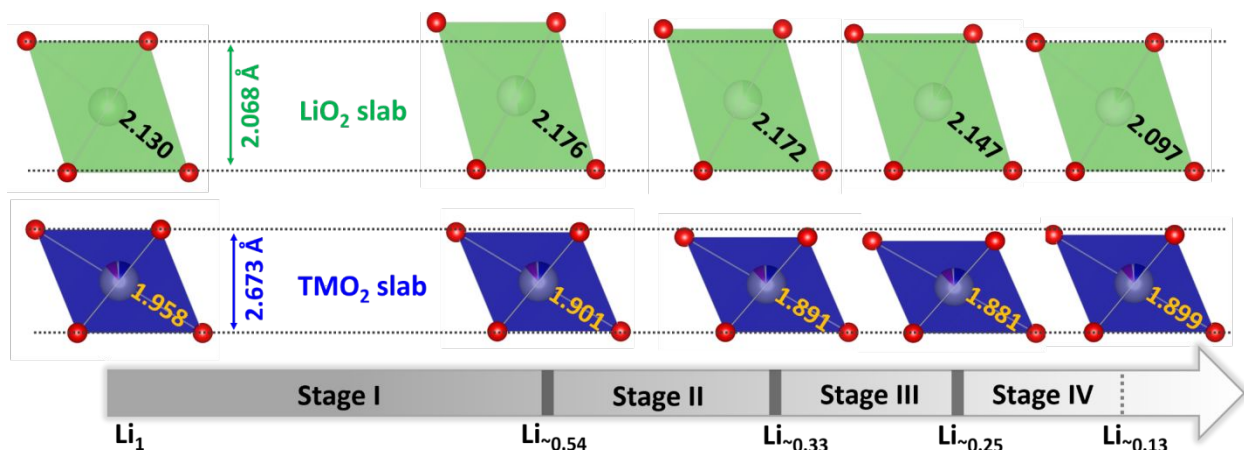

Figure 6. Summary of the four-stage structural evolution of Ni-rich cathodes during the initial charge (values from $Li_xNi_{0.8}Mn_{0.1}Co_{0.1}O_2$ are used here). In stage I ($0.45 < x < 1$ in Li_xTMO_2), Li-O bond length (in black, Å) and LiO_2 slab thickness (in olive) increase while TM-O bond length (in orange, Å) and TMO_2 slab thickness (in blue) decrease. In stage II ($0.33 < x < 0.45$), Li-O bond length and LiO_2 slab thickness plateau out. In contrast, TM-O bond length and TMO_2 slab thickness continuously decrease. In stage III ($0.25 < x < 0.33$), Li-O bond length and LiO_2 slab thickness start to decrease drastically while TM-O bond length and TMO_2 slab thickness follow the trend of previous stages. In stage IV ($x < 0.25$), Li-O bond length and LiO_2 slab thickness continue the sharp decrease. In contrast, TM-O bond length and TMO_2 slab thickness switch to the opposite direction and start to increase.

To summarize (Figure 6), there are four distinct structure transitions during the initial charge of Ni-rich cathodes (up to 4.6 V versus graphite). Region I ($0 < x < 0.55$ in $Li_{1-x}TMO_2$): Li-O bond lengths and LiO_2 slab thickness increase monotonically as a function of delithiation while TM-O bond lengths and TMO_2 slab thickness decrease; Region II ($0.55 < x < 0.67$): the change of Li-O bond length and LiO_2 slab thickness start to plateau. In contrast, TM-O bond lengths and TMO_2 slab thickness continues decreasing throughout this region. Region III ($0.67 < x < 0.75$): this region

is of great interest because it sees the collapse of cell volume (and lattice parameter *c*), sharp decrease of Li-O bond lengths and LiO_2 slab thickness, yet the TM-O bond length, TMO_2 slab thickness and interlayer O-O distance (within TMO_2 slab) continuously decrease as that in previous regions. Region IV (x > 0.75): *c*-lattice, cell volume, Li-O bond length and LiO_2 slab thickness continues collapsing. In clear contrast, TM-O bond length, TMO_2 slab thickness and interlayer O-O distance switch to the opposite direction and start to increase (Figures 5 and S44). Conventionally, TM-O bond lengths in Li-ion battery cathodes are believed to decrease during charge (oxidation) because of the decrease of TM ionic radii and the increase of TM-O covalency.[10, 48-51] The anomalous increase of TM-O bond lengths in stage IV indicates that more complicated phase transition mechanisms are involved at high SOCs (> 75%). Similar structure transition patterns of these four samples also suggests that Ni-rich cathodes are likely to follow a universal (lithium content dependent) structural transition mechanism during the first cycle regardless of Ni or substituent contents. To confirm the observation from *operando* neutron diffraction, *in situ* XAS and EXAFS data were collected for NMC811 (Figures S51-S52) during the initial charge to 4.8 V (versus Li^+/Li). The results are in good agreement with those from neutron diffraction results. The change of Ni-O bond length (Figure S51d) is consistent with the results from *operando* neutron diffraction, and it indeed shows the anomalous increase of Ni-O bond lengths above 76% delithiation. Though the onset of the anomalous elongation of Ni-O bond occurs at slightly higher degree of delithiation, the overall trend is consistent with that from neutron diffraction. The slight difference for the onset is likely routed in the different length scales probed by EXAFS and neutron Bragg diffraction. The former provides information about the very short-range/local structure while the latter probes the average structure.

3. Discussion

3.1 Origin of the anomalous structural transition at ~75% delithiation

It has been well documented in the literature that Mn and Co are in the valence state of 4+ and 3+ in the pristine NMCs or NCAs.[50-53] Thus, it is generally agreed that Ni^{2+} and Ni^{3+} co-exist in NMCs while only Ni^{3+} presents in NCAs. Numerous *in situ*/*ex situ* X-ray absorption (XAS) studies

demonstrate that Mn^{4+} remains inactive and does not contribute to the charge compensation during the entire charging process.[50, 52] This has also been confirmed in our *in situ* Mn K-edge XAS study of NMC811 during the initial charge to 4.8 V (versus Li^+/Li, Figures S52a). Although the role of Co^{3+} in charge compensation remains debatable, Co^{3+} (strictly speaking the Co *3d – O 2p* hybridized state) is widely reported to only directly contribute to the charge compensation at high degrees of delithiation.[50-52, 54] Therefore, the charge compensation mechanism in Ni-rich NMCs and NCAs are conventionally centered on Ni^{2+}/Ni^{3+} (only for NMCs) and Ni^{3+}/Ni^{4+} redox couples. Specifically, it is believed that during Li^+ removal, Ni^{2+} is first oxidized to Ni^{3+} (for NMCs) and then further oxidized to Ni^{4+}.[51, 52] The covalency between Ni and O increases as a function of delithiation, resulting in the partial charge depletion on ligand oxygen ions.[50, 52] This model successfully explains the structural changes in regions I and II (Figures 4, 5 and S44): on one hand, the screening effect (from Li^+) decreases between oxygen ions across the LiO_2 slab as Li^+ is removed from the structure, leading to much stronger electrostatic repulsions among oxygen ions across the LiO_2 slab. This drives the expansion of LiO_2 slab and leads to the increase of *c*-lattice. On the other hand, oxidation of Ni increases the covalency between Ni and ligand oxygen, which reduces the effective charge around oxygen ions and thus results in the decrease of electrostatic repulsion between oxygen ions across the LiO_2 slab. In region I ($0 < x < 0.55$), the decrease of screening effect dominates because of the relative limited charge depletion on oxygen (due to the relatively limited increase of covalency). Hence, the decrease of screening effect drives both LiO_2 slab thickness and lattice parameter *c* to increase. In region II ($0.55 < x < 0.67$), the covalency induced charge redistribution between O and Ni becomes significant, such that the electrostatic repulsion between oxygen ions across the LiO_2 slab gradually decreases and eventually surpasses the counter contribution from the decrease of the screening effect. As a result, LiO_2 slab thickness and *c*-lattice start to plateau out and then slightly decrease in this region. On the other hand, the average TM-O bond lengths and TMO_2 slab thickness decrease as a function of delithiation in both regions, in good agreement with the conventional picture of cationic redox and TM-O covalency dominated charge compensation mechanism.[50, 52] However, this classical model becomes deficient

15

in understanding the structural changes in regions III and IV. In region III ($0.67 < x < 0.75$), the almost linear collapsing of LiO_2 slab and c-lattice indicates that the electrostatic repulsion between oxygen ions across the LiO_2 slab decrease drastically. The increase of TM-O covalency alone fails to explain this dramatic charge depletion because it is expected to vary nearly linearly as a function of delithiation.[49, 55, 56] It was later pointed out that corrections for Van der Waals interaction are needed to correctly predict the anisotropic collapsing of the cell volume.[57] However, this improved model still fails to explain the anomalous increase of TM-O bond lengths in region IV ($x > 0.75$): oxidation of Ni^{3+} (or Co^{3+}) and increase of Ni (Co)-O covalency will both lead to the decrease of average TM-O bond lengths because of the reduced cation ionic radii and the increased hybridization between high valence cation $3d$ orbital and oxygen $2p$ orbital.[58, 59] Taken together, this suggests that the charge compensation and structural transition mechanism of Ni-rich cathodes are more complex after removing more than ~0.75 Li^+ (stage IV).

One plausible explanation for this anomalous increase of TM-O bond lengths is the direct oxidation of lattice oxygen ions. It is well documented in the literature that high-valent late $3d$ transition metal oxides, such as cuprates and nickelates, belong to the so-called small or negative charge transfer gapped materials according to the ZSA model,[60-63] where the ligand-to-TM charge-transfer energy (Δ) is near zero or negative (supporting information S3 and Figure S45). Therefore, hole doping in these systems creates electron holes on the ligand oxygen $2p$ dominated bands (*ligand-hole* character) instead of on the conventional TM $3d$ dominated states.[63, 64] Removing Li^+ from Ni-rich cathodes (e.g., $Li_{1-x}Ni_{0.8}Mn_{0.1}Co_{0.1}O_2$) continuously decreases the charge transfer gap, similar to increasing the amounts (y) of aliovalent dopant in $La_{2-y}Sr_yNiO_4$.[63-65] This process eventually pushes the empty Ni $3d$ dominant e_g^* states to overlap with itinerant oxygen $2p$ (dominated) bands (Figure 7, $x > 0.75$). A variety of fiercely debated scenarios have been proposed in the literature regarding this overlap: (1) a metallic state by merging these two states; (2) an insulating state due to the re-hybridization of these two states; and (3) a more complicated spin pairing state resembles that of the Zhang-Rice singlets in the hole-doped cuprates or π-type singlet states in CrO_2.[64, 66, 67] We further carried out DFT calculation of the electronic structure (Figure

S55) of $LiNiO_2$ (the parent compound of Ni-rich cathodes) at the pristine stage, 75% delithiation (the onset of the anomalous increase of average Ni-O bond lengths) and the fully delithiated state. It can be seen that the front of the valence band is dominated by oxygen 2p character in the 75% and fully charged Li_xNiO_2. It is also worth noting that there is an intermediate state/band (though not fully separated from the major valence band) in the $Li_{0.25}NiO_2$, suggesting that the formation of spin singlet (p-d rehybridized) states may be the most likely electronic structure in stages III and IV. Although this result cannot definitely rule out the other two plausible electronic structures for the deeply charged NMCs and NCA, all three models share two common features: (1) the electron holes (due to Li^+ removal) are created on the oxygen *2p* dominated $t_{2g}*$ bands instead of the conventional TM 3d dominated states (i.e., Ni e_g*); and (2) electrons are partially transferred from the oxygen dominant $t_{2g}*$ bands to the empty Ni 3d dominant e_g* states, in other words, there is a partial electron transfer from the weak $\pi*$ (oxygen *2p* dominant) state to the strong $\sigma*$ (strongly *d-p* hybridized) state. Thus, at stage IV, in addition to the creation of holes on the itinerant oxygen *2p* bands, there is also an inevitable electron transfer from the filled bands with oxygen *2p* parentage to the empty Ni *3d* dominated anti-bonding states. Such a charge transfer process increases the average Ni-O bond lengths. In contrast, oxidation of lattice oxygen ions decreases the average TM-O bond lengths, which has been well documented in various hole-doped cuprates.[65, 68] These two opposite effects compete and the relative strength decides the overall trend of average TM-O bond lengths. In Ni-rich cathodes, the former effect is stronger and leads to the increase of average TM(Ni)-O bond lengths. Interestingly, similar abnormal increase of average Ni-O bond length has been observed in the over-doped $La_{2-y}Sr_yNiO_4$ when y exceeds 1.4,[65] highlighting the similarity between chemical substitution and electrochemical delithiation (or oxidation) induced hole doping in high-valent nickelates. Moreover, it must be stressed that the current model is in excellent agreement with the recent observations of oxidized oxygen features (beyond the TM-O hybridization) in Resonant Inelastic X-ray Scattering (RIXS) studies of $LiNiO_2$ and NMC/NCA cathodes at high SOCs.[50, 54] Taken together, the current observation provides robust structural evidences that lattice oxygen redox dominates the charge compensation in Ni-

rich cathodes at high SOCs (x > 0.75). Further fundamental theoretical work is highly desired to underpin the nature of oxidized oxygen ions in this strongly correlated system, especially how the intermediate rehybridized band
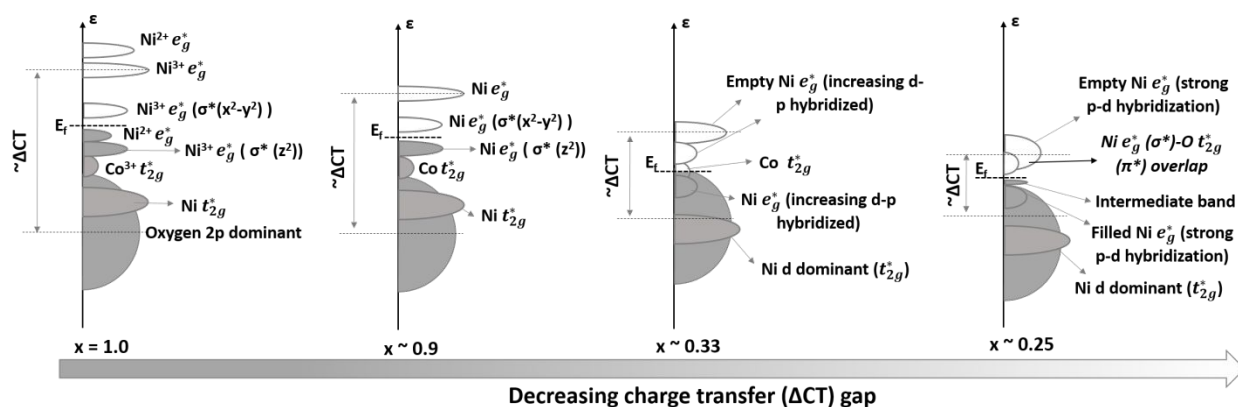

Figure 7. Schematic of the density of states of Ni-rich cathodes ($Li_xNi_{0.8}Mn_{0.1}Co_{0.1}O_2$) at four critical state of charges.

3.1 Implications

Since the oxidized lattice oxygen ions are likely metastable and they are also strong oxidizer, they are expected to highly active and maybe reduced in contacting with organic solvents in electrolytes.[69, 70] To further confirm this model, we carried out *operando* gas analysis to monitor the O_2 release during the initial charge of NMCs/NCA (to 4.8 V versus Li^+/Li) (Figure 6). The onsets of O_2 release indeed match well with the onset of the emerge of stage IV for all four compounds. In addition, the onset of O_2 release increases slightly from 74% in NMC811/NCA to 79% in NMC532 (Figure 8), highlighting that higher concentrations of Mn/Co are indeed beneficial for stabilizing the oxidized lattice oxygen ions (e.g., singlet pairs in scenario 3). However, the exact amount of the released oxygen gas is determined by many factors besides the amount of oxidized oxygen ions, such as the level of stabilization (of oxidized oxygen ions) on the cathode surface/subsurface. It is known that Mn^{4+} is particularly beneficial for stabilizing the

18

oxidized lattice oxygen ions (e.g., the Mn and Li excess cathodes),[71] this is because of a plausible stabilization mechanism similar to the conjugated π-bonding in the aromatic organic
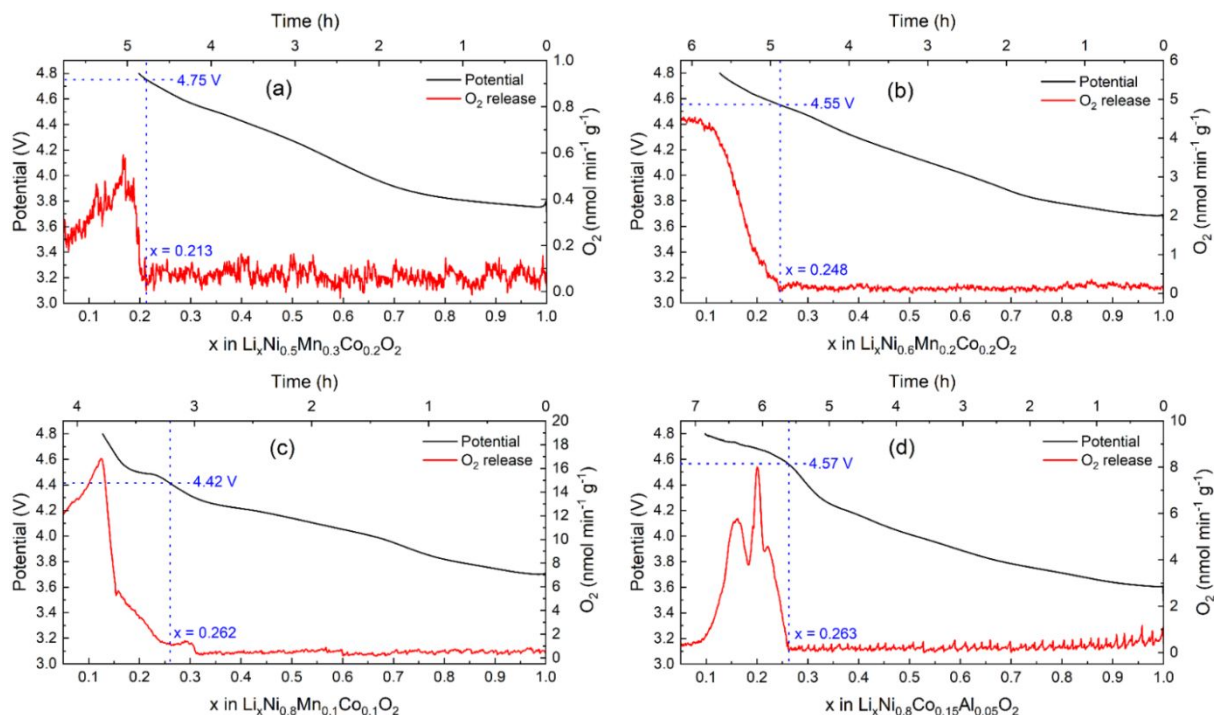

Figure 8. *In situ* O_2 gas release of (a) NMC532, (b) NMC622, (c) NMC811 and (d) NCA half-cell during the initial charge to 4.8 V (versus Li^+/Li).

compounds. This has recently been confirmed both experimentally and theoretically in the model compound $Na_2Mn_3O_7$.[72, 73] Thus, it is expected that compounds with higher concentrations of Mn and Co release less oxygen gases. Nevertheless, it should be emphasized that the amount of O_2 gas is very limited, suggesting that the O_2 evolution is a gradual process and it is likely started from the surface/subsurface (those directly exposed to the electrolyte) rather than from the bulk. This is indeed consistent with the fact that the bulk transition is fully reversible during the initial discharge (Figures 4 and 5). Moreover, this observation resonates very well with the recent report from Dahn et al.,[17] where a universal decline of capacity retention is found for 26 different Ni-rich cathodes when more than 210 mAh/g capacities are used during the initial cycle. In all, this study highlights the importance of stabilizing oxidized lattice oxygen ions, especially those on the

surface/subsurface, in Ni-rich cathodes at SOCs above 75%. This may be achieved by surface doping/substituting of early TM cations (e.g., Ti^{4+}), which can form strong ionic bonding with oxygen but with large positive charge transfer gaps ($\varepsilon_{TM3d} > \varepsilon_{O2p}$).[69] Reducing the amounts of surface area and surface defects (e.g., using single crystalline sample) should also help to mitigate this side effect.[13]

4. Conclusion

A universal four-stage structural evolution of Ni-rich cathodes (irrespective of the Ni and substituent contents) is revealed by *operando* neutron diffraction during the initial cycle. Particularly, an anomalous increase of average TM-O bond lengths in Ni-rich cathodes is observed for the first time when more than ~ 0.75 Li^+ are removed. This anomaly is likely originated from the direct oxidation of lattice oxygen ions, which is associated with the drastic decrease of charge transfer gap between the empty Ni *3d* dominated states and the filled oxygen *2p* bands. It induces partial electron transfer from the weak π^* (primarily oxygen *2p* character) states to the strong σ^* (strongly *d-p* hybridized) state, leading to the elongation of average TM(Ni)-O bond lengths. This transition is found to be strongly correlated with oxygen gas release and the universal decline of capacity retention in Ni-rich cathodes. In all, this study reveals that oxygen redox-induced structural transition might be the universal driving force underlying the severe capacity degradation of Ni-rich cathodes charged to high SOCs, providing fundamental insights to stabilize oxidized oxygen ions for stable cycling of layered oxide cathodes. More generally, the discovery of the anomalous increase of TM-O bond lengths during charge (oxidation) of Ni-rich cathodes may stimulate broad interests in re-visiting the charge-transfer mechanism in late transition metal oxides during oxidation/reduction.

5. Experiment and methods

***In situ* battery cells:** The newly designed *in situ* cells are shown in Figure S1. Thin walled quartz tubes are used as cell body to allow easy electrode alignments (transparent) and to prevent internal short circuit (insulating). In addition, the use of thin walled quartz tube enables easy fabrication

of large amounts of customized *in situ* cells to allow both quantitative and high-throughput *operando* neutron diffraction experiments. $LiNi_{0.5}Mn_{0.3}Co_{0.2}O_2$ (Toda America), $LiNi_{0.6}Mn_{0.2}Co_{0.2}O_2$, (Targrey) $LiNi_{0.8}Mn_{0.1}Co_{0.1}O_2$ (Targrey) and $LiNi_{0.8}Co_{0.15}Al_{0.05}O_2$ (MTI Corporation) were used as the cathode active materials. The cathode electrodes were prepared by slurry casting and drying on Al foil with a composition of active materials/carbon black/PVDF binder of 92/4/4 wt%. Graphite anodes were prepared by similar method on Cu foil. Cathodes and anodes were separated by a porous polymer separator (Celgard 2325) and rolled into cylindrical shape. The "jelly rolls" were then transferred into quartz tubes and sealed in Ar-filled glove boxes after adding electrolytes of 1.2 M $LiPF_6$ in EC (ethylene carbonate)/EMC (Ethyl methyl carbonate) 30/70 wt%. Moreover, since these in situ cells are mounted and cycled vertically (Figures 1 and S1), most of the residual electrolyte is concentrated at the bottom of the cell which is out of the direct neutron beam. Therefore, this configuration minimizes the amounts of illuminated electrolytes and significantly reduces the incoherent scattering signal from H. This essentially allows the collection of structure refinable quality data without using deuterated electrolytes.

***In situ* and *ex situ* neutron diffraction**: Neutron diffraction data were collected at the NOMAD beamline at the Spallation Neutron Source, Oak Ridge National Laboratory. NOMAD is one of the fastest neutron diffractometers in the world.[38] The very high pulsed neutron flux and large detector coverage enables fast data collection of relatively small amounts of samples (tens to hundreds of milligrams), which is crucial for both *in situ* battery experiments and *ex situ* studies of cycled battery electrode materials. For the ex situ experiment, about 0.3 g powder samples of pristine and 4.6 V charged (versus graphite) NMCs and NCA were loaded into 3 mm quartz capillaries and sealed. These sealed capillaries were then mounted on a customized bracket where a maximum of 10 samples can be loaded. The bracket was mounted onto a linear motor-controlled shifter for data collection. Four 24 min scans were collected for each sample and then summed together to improve statistics. Signal from the empty quartz capillary was subtracted as background from the sample measurement and data were normalized by the scattering intensity from a 6 mm (diameter) vanadium rod to correct for detector efficiencies. For *in situ/operando* experiment, four

in situ cells were mounted vertically on the bracket (Figures 1 and S1). These *in situ* cells were then connected to a Biologic VMP3 potentiostat (Figure S1). These in situ cells were cycled at a C/10 rate between 4.6 V and 2.8 V (versus graphite). 4 min scans were collected for each cell in a sequential manner and the average motor moving time between the neighboring cells was around 20 s. Accordingly, diffraction data were collected every 17.3 min for each in situ cell and a total of 33-36 scans were collected during the initial charge. About 30 -32 scans were collected during the initial discharge. This corresponds to an extraction/insertion of 0.022- 0.025 Li^+ per formula per scan.

Structure refinements: Structure refinements were carried out using TOPAS v6 software.[74] Time-of-flight (TOF) were converted to d-spacing using the conventional second order polynomial $TOF = ZERO + DIFC*d + DIFA*d^2$, where ZERO is a constant, DIFC is the diffractometer constant and DIFA is an empirical term to correct for sample displacements and absorption induced peak shifts. ZERO and DIFC were determined from the refinement of a standard NIST Si-640e data set and held fixed, while DIFA was allowed to vary during refinements to account for the sample displacements. For the low-resolution frames (bank 2 and 3), a back to back exponential function convoluted with a symmetrical Gaussian function was used to describe the peak profile. For the high-resolution frames (bank 4 and 5), the moderator induced line profile was modeled using a modified Ikeda-Carpenter-David function.[75-77] Lorenz polarization is corrected by multiplying $d^4 \sin\theta$.[76] Absorption correction is critical for reliable structure refinements using TOF neutron diffraction data of absorbing samples, such as the current in situ cells. This differs from the constant wavelength diffraction experiments where the absorption induced intensity dampening can be effectively compensated by introducing very small or negative atomic displacement parameters.[78, 79] The complex configuration of jelly roll cells prevents reliable numerical calculation of absorption factors. Therefore, absorption correction was carried out using the empirical Lobanov formula.[76, 80] This method has been proven to be effective for absorption correction of multiple frame NOMAD data, as can be seen from the example of structure refinements of the [11]B enriched NIST standard LaB_6 (99% [11]B, Figure S46). Significant anisotropic

22

peak broadening has been observed for the pristine graphite phase. This is likely caused by the presence of stacking faults of graphene layers in the graphite. It is difficult to accurately model the nature of stacking faults and faulting probability using the current *operando* diffraction data, especially considering that stacking sequences (of graphene layers) will change after Li^+ intercalation/deintercalation. Thus, a phenomenological anisotropic strain broadening model was incorporated during the refinement.[81] No obvious anisotropic peak broadening was observed for the pristine cathode materials which is consistent with the *ex situ* measurements of powder samples (Figures S2-S5). To test the sensitivity of these *in situ* data toward lithium, Fourier difference maps were generated from refinements using the lithium removed TMO_2 (S.G. R-3m) structure. Clear residual densities of negative nuclear scattering lengths are identified (Figure S47) and the residual density position matches very well with the actual lithium position (000) in the O3-type structure, suggesting that the current in situ data are indeed able to reliably locate Li^+ positions. This is further confirmed by the significant improvements of fit quality after adding lithium into the structure refinements (Figure S47).

Parametric structure refinements were carried out for all four cells (multiple components) in TOPAS v6. The weightings of Cu and Al were fixed to values refined from the initial patterns (before charging). Since the atomic displacement and site occupancy of Li^+ are strongly correlated, and both vary as a function of delithiation, it is difficult to reliably refine both parameters simultaneously. For the current study, we have tested refining Li occupancy with fixed atomic displacements and vice versa. Although the overall trend of refined lithium occupancy decreases (Figure S48), it varies from the values obtained from electrochemistry data, especially at high degrees of delithiation. This is likely rooted in the fact that lithium mobility changes during lithium intercalation/deintercalation.[44] Since electrochemistry provides accurate information about average lithium concentration, it is thus reasonable to fix the lithium occupancy (to the values obtained from electrochemistry data) while refining the atomic displacement parameters. Anisotropic peak broadening becomes significant for all four samples at SOCs above 50%. Therefore, a phenomenological anisotropic strain broadening model (Stephen's peak shape) was

incorporated during sequential refinements. We found that refining S004 term alone (trigonal_high) can adequately fit the anisotropic broaden peaks, indicating that this anisotropic peak broadening is very likely caused by the stacking disorder along *c*-axis.[46] The refined values of S004 are shown as a function of the degree of delithiation in Figure S49. It indeed confirms that the anisotropic peak broadening emerges at about 50% delithiation. No noticeable changes of Ni/Li anti-site defects were found during the entire charge and discharge process. We further confirmed this conclusion from structure refinements using the powder samples recovered after charging to 4.6 V (versus graphite, Table S16-S20). We also tested the possibility of Ni migrates to the tetrahedral site in the Li layer, no noticeable improvements of fit quality were found.

***In situ* gas analysis**: *In situ* gas analysis was performed with a mass spectrometer (Shimadzu GCMS-QP2020 NX) directly connecting to pouch cells with a sampling column. The details of the experimental setup can be found in a previous work.[82] Single layer pouch cells with LNO-based cathodes and lithium foil anodes were fabricated in a dry room with dew point of less than -50 °C (0.1% RH). Electrolyte used in the pouch cells was 1.2M $LiPF_6$ in ethylene carbonate and diethyl carbonate (EC/EMC) (3:7 wt%). The pouch cells were connected to MS and potentiostat while being placed in a 30 °C environmental chamber. Mass spectrum was obtained every 10 seconds using continuous scan mode within scan range of m/z 2-100. The operation parameters of the MS are summarized in Table S21. In our investigated system, m/z 32 is unique to O_2 with very minor contributions from EMC in the electrolyte. After removing the contribution of m/z 32 from electrolyte, the O_2 evolution rates were quantified by calibration of standard gases.

In situ X-ray absorption spectroscopy: In-situ Mn, Co and Ni K-edge hard X-ray absorption spectroscopy (XAS) of $LiNi_{0.8}Mn_{0.1}Co_{0.2}O_2$ (versus Li^+/Li) was carried out at beamline 7-BM (QAS) in National Synchrotron Light Source II (NSLS II) at Brookhaven National Laboratory. The in-situ XAS data were collected in transmission mode. Reference spectra of transition metal elements were simultaneously recorded using metal foil for energy calibration. The obtained X-ray absorption near-edge structure (XANES) and extended X-ray absorption fine structure (EXAFS) spectra were analyzed using the Athena and Artemis software package.[83]

24

DFT calculation: All DFT calculations were performed with the Vienna ab initio simulation package (VASP) with projector augmented wave (PAW) approach.[84, 85] For the crystal structure relaxation of layer $Li_{1-x}NiO_2$ (x=0, 0.75, 1), the generalized gradient approximation (GGA) type exchange–correlation functional in the parameterization of Perdew, Burke, and Ernzerhof (PBE) was adopted,[86] and Hubbard U type correction was used with effective U value of 6 eV for Ni.[87] As reported in previous research, a 2×2 supercell containing a ordered in-plane Li-Vacancy configuration was used for the $Li_{0.25}NiO_2$ model.[88, 89] The model structures were considered reaching equilibrium state until forces felt by each of the atoms were well converged below 0.005 eV $Å^{-1}$. For the calculation of electronic structure for the relaxed structure, the Heyd–Scuseria–Ernzerhof (HSE) hybrid functional was adopted, which is reported to give more accurate results than the common DFT+U functional, especially in describing empty states above Fermi level.[90, 91] For HSE type functional, the choice of mixing parameter is important since it directly determines how much electron exchange is taken into account and relates to the accuracy of results closely. Rigorous approach to obtain mixing parameter is nonempirically tuning the fraction of mixing as suggested by Kronik and co-workers.[92, 93] For $LiNiO_2$, previous theoretical studies had concluded that the mixing parameter of 0.2 give an overall better description in regard of calculated charging voltage and band gap.[90] Therefore, in the calculation of this work, the mixing parameter of 0.2 was taken for consistency. For all calculations, the cutoff of the plane wave basis was 520 eV. A k-mesh with the density of one point per $\approx$0.03 $Å^{-3}$ was generated using the Monkhorst–Pack method to ensure the precision of the calculated total energy.

Acknowledgements

Conflicts of interest

There are no conflicts to declare.

References:

1. M. Armand and J.-M. Tarascon, *Nature*, 2008, **451**, 652-657.
2. M. S. Whittingham, *Chem. Rev.*, 2004, **104**, 4271-4302.
3. C. Masquelier and L. Croguennec, *Chem. Rev.*, 2013, **113**, 6552-6591.
4. J. B. Goodenough and Y. Kim, *Chem. Mater.*, 2010, **22**, 587-603.
5. M. Bianchini, M. Roca‑Ayats, P. Hartmann, T. Brezesinski and J. Janek, *Angew. Chem. Int. Ed.*, 2019, **58**, 10434-10458.
6. Z. Lu, D. MacNeil and J. Dahn, *Electrochem. Solid-State Lett.* , 2001, **4**, A200.
7. C. Chen, J. Liu, M. Stoll, G. Henriksen, D. Vissers and K. Amine, *J. Power Sources*, 2004, **128**, 278-285.
8. A. Manthiram, J. C. Knight, S.-T. Myung, S.-M. Oh and Y.-K. Sun, *Adv. Energy Mater.*, 2016, **6**, 1501010.
9. J. Kim, H. Lee, H. Cha, M. Yoon, M. Park and J. Cho, *Adv. Energy Mater.*, 2018, **8**, 1702028.
10. H.-H. Ryu, K.-J. Park, C. S. Yoon and Y.-K. Sun, *Chem. Mater.*, 2018, **30**, 1155-1163.
11. K.-J. Park, J.-Y. Hwang, H.-H. Ryu, F. Maglia, S.-J. Kim, P. Lamp, C. S. Yoon and Y.-K. Sun, *ACS Energy Lett.*, 2019, **4**, 1394-1400.
12. H. Liu, M. Wolf, K. Karki, Y.-S. Yu, E. A. Stach, J. Cabana, K. W. Chapman and P. J. Chupas, *Nano Lett.*, 2017, **17**, 3452-3457.
13. Y. Bi, J. Tao, Y. Wu, L. Li, Y. Xu, E. Hu, B. Wu, J. Hu, C. Wang, J.-G. Zhang, Y. Qi and J. Xiao, *Science*, 2020, **370**, 1313-1317.
14. P.-C. Tsai, B. Wen, M. Wolfman, M.-J. Choe, M. S. Pan, L. Su, K. Thornton, J. Cabana and Y.-M. Chiang, *Energy Environ. Sci.*, 2018, **11**, 860-871.
15. L. Romano Brandt, J.-J. Marie, T. Moxham, D. P. Förstermann, E. Salvati, C. Besnard, C. Papadaki, Z. Wang, P. G. Bruce and A. M. Korsunsky, *Energy Environ. Sci.*, 2020, **13**, 3556-3566.
16. W. Li, H. Y. Asl, Q. Xie and A. Manthiram, *J. Am. Chem. Soc.*, 2019, **141**, 5097-5101.
17. H. Li, A. Liu, N. Zhang, Y. Wang, S. Yin, H. Wu and J. R. Dahn, *Chem. Mater.*, 2019, **31**, 7574-7583.
18. C. Xu, K. Märker, J. Lee, A. Mahadevegowda, P. J. Reeves, S. J. Day, M. F. Groh, S. P. Emge, C. Ducati, B. Layla Mehdi, C. C. Tang and C. P. Grey, *Nat. Mater.*, 2021, 20, 84-92.
19. J. Li, L. E. Downie, L. Ma, W. Qiu and J. Dahn, *J. Electrochem. Soc.*, 2015, **162**, A1401.
20. N. Y. Kim, T. Yim, J. H. Song, J.-S. Yu and Z. Lee, *J. Power Sources*, 2016, **307**, 641-648.
21. R. Robert, C. Bünzli, E. J. Berg and P. Novák, *Chem. Mater.*, 2015, **27**, 526-536.

22.   F. Lin, D. Nordlund, Y. Li, M. K. Quan, L. Cheng, T.-C. Weng, Y. Liu, H. L. Xin and M. M. Doeff, *Nat. Energy*, 2016, **1**, 1-8.
23.   J. A. Gilbert, I. A. Shkrob and D. P. Abraham, *J. Electrochem. Soc.*, 2017, **164**, A389.
24.   F. Lin, I. M. Markus, D. Nordlund, T.-C. Weng, M. D. Asta, H. L. Xin and M. M. Doeff, *Nat. Commun.*, 2014, **5**, 1-9.
25.   R. Jung, M. Metzger, F. Maglia, C. Stinner and H. A. Gasteiger, *J. Electrochem. Soc.*, 2017, **164**, A1361.
26.   C. Tian, D. Nordlund, H. L. Xin, Y. Xu, Y. Liu, D. Sokaras, F. Lin and M. M. Doeff, *J. Electrochem. Soc.*, 2018, **165**, A696.
27.   J. Wandt, A. T. Freiberg, A. Ogrodnik and H. A. Gasteiger, *Mater. Today*, 2018, **21**, 825-833.
28.   G. G. Amatucci, J. M. Tarascon and L. C. Klein, *J. Electrochem. Soc.*, 1996, **143**, 1114-1123.
29.   G. Liang, C. Didier, Z. Guo, W. K. Pang and V. K. Peterson, *Adv. Mater.*, 2020, **32**, 1904528.
30.   F. Rosciano, M. Holzapfel, W. Scheifele and P. Novák, *J. Appl. Crystallogr.*, 2008, **41**, 690-694.
31.   W. K. Pang, V. K. Peterson, N. Sharma, J.-J. Shiu and S.-h. Wu, *Chem. Mater.*, 2014, **26**, 2318-2326.
32.   N. Sharma, V. K. Peterson, M. M. Elcombe, M. Avdeev, A. J. Studer, N. Blagojevic, R. Yusoff and N. Kamarulzaman, *J. Power Sources*, 2010, **195**, 8258-8266.
33.   M. Bianchini, E. Suard, L. Croguennec and C. Masquelier, *J. Phys. Chem. C*, 2014, **118**, 25947-25955.
34.   V. Baran, M. J. Mühlbauer, M. Schulz, J. Pfanzelt and A. Senyshyn, *J. Energy Storage*, 2019, **24**, 100772.
35.   D. Liu, Z. Shadike, R. Lin, K. Qian, H. Li, K. Li, S. Wang, Q. Yu, M. Liu, S. Ganapathy, X. Qin, Q.-H. Yang, M. Wagemaker, F. Kang, X.-Q. Yang and B. Li, *Adv. Mater.*, 2019, **31**, 1806620.
36.   B. Song, G. M. Veith, J. Park, M. Yoon, P. S. Whitfield, M. J. Kirkham, J. Liu and A. Huq, *Chem. Mater.*, 2018, **31**, 124-134.
37.   W. Li, E. M. Erickson and A. Manthiram, *Nat. Energy*, 2020, **5**, 26-34.
38.   J. Neuefeind, M. Feygenson, J. Carruth, R. Hoffmann and K. K. Chipley, *Nucl. Instrum. Methods Phys. Res., B*, 2012, **287**, 68-75.
39.   S. Calder, K. An, R. Boehler, C. R. D. Cruz, M. D. Frontzek, M. Guthrie, B. Haberl, A. Huq, S. A. J. Kimber, J. Liu, J. J. Molaison, J. Neuefeind, K. Page, A. M. d. Santos, K. M. Taddei, C. Tulk and M. G. Tucker, *Rev. Sci. Instrum.*, 2018, **89**, 092701.
40.   R. t. Shannon and C. Prewitt, *Acta Crystallogr. B*, 1970, **26**, 1046-1048.
41.   K. Kang, Y. S. Meng, J. Breger, C. P. Grey and G. Ceder, *Science*, 2006, **311**, 977-980.
42.   L. Yin, Z. Li, G. S. Mattei, J. Zheng, W. Zhao, F. Omenya, C. Fang, W. Li, J. Li, Q. Xie, E. M. Erickson, J.-G. Zhang, M. S. Whittingham, Y. S. Meng, A. Manthiram and P. G. Khalifah, *Chem. Mater.*, 2019, **32**, 1002-1010.

43.   J. Zheng, G. Teng, C. Xin, Z. Zhuo, J. Liu, Q. Li, Z. Hu, M. Xu, S. Yan and W. Yang, *J. Phys. Chem. Lett.*, 2017, **8**, 5537-5542.

44.   K. Märker, P. J. Reeves, C. Xu, K. J. Griffith and C. P. Grey, *Chem. Mater.*, 2019, **31**, 2545-2554.

45.   A. Grenier, H. Liu, K. M. Wiaderek, Z. W. Lebens-Higgins, O. J. Borkiewicz, L. F. Piper, P. J. Chupas and K. W. Chapman, *Chem. Mater.*, 2017, **29**, 7345-7352.

46.   L. Croguennec, C. Pouillerie, A. Mansour and C. Delmas, *J. Mater. Chem.*, 2001, **11**, 131-141.

47.   G. W. Stinton and J. S. Evans, *J. Appl. Crystallogr.*, 2007, **40**, 87-95.

48.   W.-S. Yoon, K.-B. Kim, M.-G. Kim, M.-K. Lee, H.-J. Shin, J.-M. Lee, J.-S. Lee and C.-H. Yo, *J. Phys. Chem. B*, 2002, **106**, 2526-2532.

49.   A. Van der Ven, M. Aydinol, G. Ceder, G. Kresse and J. Hafner, *Phys. Rev. B*, 1998, **58**, 2975.

50.   Z. W. Lebens-Higgins, N. V. Faenza, M. D. Radin, H. Liu, S. Sallis, J. Rana, J. Vinckeviciute, P. J. Reeves, M. J. Zuba, F. Badway, N. Pereira, K. W. Chapman, T.-L. Lee, T. Wu, C. P. Grey, B. C. Melot, A. Van Der Ven, G. G. Amatucci, W. Yang and L. F. J. Piper, *Mater. Horiz.*, 2019, **6**, 2112-2123.

51.   W.-S. Yoon, M. Balasubramanian, K. Y. Chung, X.-Q. Yang, J. McBreen, C. P. Grey and D. A. Fischer, *J. Am. Chem. Soc.*, 2005, **127**, 17479-17487.

52.   A. O. Kondrakov, H. Geßwein, K. Galdina, L. de Biasi, V. Meded, E. O. Filatova, G. Schumacher, W. Wenzel, P. Hartmann, T. Brezesinski and J. Janek, *J. Phys. Chem. C*, 2017, **121**, 24381-24388.

53.   Y. Tsai, B. Hwang, G. Ceder, H. Sheu, D. Liu and J. Lee, *Chem. Mater.*, 2005, **17**, 3191-3199.

54.   G. H. Lee, J. Wu, D. Kim, K. Cho, M. Cho, W. Yang and Y. M. Kang, *Angew. Chem. Int. Ed.*, 2020, **59**, 8681-8688.

55.   M. Dixit, B. Markovsky, F. Schipper, D. Aurbach and D. T. Major, *J. Phys. Chem. C*, 2017, **121**, 22628-22636.

56.   A. Chakraborty, S. Kunnikuruvan, S. Kumar, B. Markovsky, D. Aurbach, M. Dixit and D. T. Major, *Chem. Mater.*, 2020, **32**, 915-952.

57.   M. Aykol, S. Kim and C. Wolverton, *J. Phys. Chem. C*, 2015, **119**, 19053-19058.

58.   R. D. Shannon and C. T. Prewitt, *Acta Crystallographica Section B*, 1969, **25**, 925-946.

59.   F. A. Cotton, G. Wilkinson, C. A. Murillo, M. Bochmann and R. Grimes, *Advanced Inorganic Chemistry*, Wiley New York, 1988.

60.   J. Zaanen, G. Sawatzky and J. Allen, *Phys. Rev. Lett.*, 1985, **55**, 418.

61.   V. Bisogni, S. Catalano, R. J. Green, M. Gibert, R. Scherwitzl, Y. Huang, V. N. Strocov, P. Zubko, S. Balandeh, J.-M. Triscone, G. Sawatzky and T. Schmitt, *Nat. Commun.*, 2016, **7**, 13017.

62.   A. E. Bocquet, T. Mizokawa, T. Saitoh, H. Namatame and A. Fujimori, *Phys. Rev. B*, 1992, **46**, 3771-3784.

63.   M. Imada, A. Fujimori and Y. Tokura, *Rev. Mod. Phys.*, 1998, **70**, 1039.

64.   D. Khomskii, *Transition metal compounds*, Cambridge University Press, 2014.

65.   Y. Takeda, R. Kanno, M. Sakano, O. Yamamoto, M. Takano, Y. Bando, H. Akinaga, K. Takita and J. Goodenough, *Mater. Res. Bull.*, 1990, **25**, 293-306.

66.   F. Zhang and T. Rice, *Phys. Rev. B*, 1988, **37**, 3759.

67.   M. Korotin, V. Anisimov, D. Khomskii and G. Sawatzky, *Phys. Rev. Lett.*, 1998, **80**, 4305.

68.   T. Kamiyana, F. Izumi, H. Asano, H. Takagi, S. Uchida, Y. Tokurs, E. Takayama-Muromachi, M. Matsuda, Y. Endoh and Y. Hidaka, *Physica C: Superconductivity*, 1990, **172**, 120-126.

69.   J.-N. Zhang, Q. Li, C. Ouyang, X. Yu, M. Ge, X. Huang, E. Hu, C. Ma, S. Li, R. Xiao, W. Yang, Y. Chu, Y. Liu, H. Yu, X.-Q. Yang, X. Huang, L. Chen and H. Li, *Nat. Energy*, 2019, **4**, 594-603.

70.   E. Hu, X. Yu, R. Lin, X. Bi, J. Lu, S. Bak, K.-W. Nam, H. L. Xin, C. Jaye, D. A. Fischer, K. Amine and X.-Q. Yang, *Nat. Energy*, 2018, **3**, 690-698.

71.   E. Zhao, M. Zhang, X. Wang, E. Hu, J. Liu, X. Yu, M. Olguin, T. A. Wynn, Y. S. Meng, K. Page, F. Wang, H. Li, X.-Q. Yang, X. Huang and L. Chen, *Energy Storage Materials*, 2020, **24**, 384-393.

72.   B. Song, M. Tang, E. Hu, O. J. Borkiewicz, K. M. Wiaderek, Y. Zhang, N. D. Phillip, X. Liu, Z. Shadike, C. Li, L. Song, Y.-Y. Hu, M. Chi, G. M. Veith, X.-Q. Yang, J. Liu, J. Nanda, K. Page and A. Huq, *Chem. Mater.*, 2019, **31**, 3756-3765.

73.   D. A. Kitchaev, J. Vinckeviciute and A. Van der Ven, *J. Am. Chem. Soc.*, 2021, **143**, 1908-1916.

74.   A. A. Coelho, *J. Appl. Crystallogr.*, 2018, **51**, 210-218.

75.   S. Ikeda and J. M. Carpenter, *Nucl. Instrum. Methods. Phys. Res. A*, 1985, **239**, 536-544.

76.   A. C. Larson and R. B. Von Dreele, *Report LAUR*, 1994, 86-748.

77.   R. A. Young, *The rietveld method*, Oxford university press Oxford, 1993.

78.   K. Rouse, M. Cooper, E. York and A. Chakera, *Acta Crystallogr. A*, 1970, **26**, 682-691.

79.   A. Hewat, *Acta Crystallogr. A*, **35**, 248-248.

80.   N. N. A. d. V. Lobanov, L., 6th European Powder Diffraction Conference, 22-25 August 1988, Budapest, Hungary, Abstract P12-16.1988.

81.   P. W. Stephens, *J. Appl. Crystallogr.*, 1999, **32**, 281-289.

82.   L. Geng, D. L. Wood III, S. A. Lewis Sr, R. M. Connatser, M. Li, C. J. Jafta and I. Belharouak, *J. Power Sources*, 2020, **466**, 228211.

83.   B. Ravel and M. Newville, *J. Synchrotron Radiat.   J Synchrotron Radiat*, 2005, **12**, 537-541.

84.   G. Kresse and J. Furthmüller, *Computational Materials Science*, 1996, **6**, 15-50.

85.   P. E. Blöchl, *Phys. Rev. B*, 1994, **50**, 17953-17979.

86.   J. P. Perdew, K. Burke and M. Ernzerhof, *Phys. Rev. Lett.*, 1996, **77**, 3865.

87.   A. Jain, G. Hautier, C. J. Moore, S. Ping Ong, C. C. Fischer, T. Mueller, K. A. Persson and G. Ceder, *Computational Materials Science*, 2011, **50**, 2295-2310.

88.   M. A. y de Dompablo, A. Van der Ven and G. Ceder, *Phys. Rev. B*, 2002, **66**, 064112.

89.   M. A. y de Dompablo and G. Ceder, *J. Power Sources*, 2003, **119**, 654-657.

90.   D.-H. Seo, A. Urban and G. Ceder, *Phys. Rev. B*, 2015, **92**, 115118.
91.   J. Heyd and G. E. Scuseria, *The Journal of chemical physics*, 2004, **121**, 1187-1192.
92.   M. E. Foster and B. M. Wong, *Journal of chemical theory and computation*, 2012, **8**, 2682-2687.
93.   S. Refaely-Abramson, M. Jain, S. Sharifzadeh, J. B. Neaton and L. Kronik, *Phys. Rev. B*, 2015, **92**, 081204.